2010

Missing-iron problem and Type Ia supernova enrichment of hot gas in galactic spheroids

S Tang

QD Wang
University of Massachusetts - Amherst

Follow this and additional works at: https://scholarworks.umass.edu/astro_faculty_pubs

Part of the Astrophysics and Astronomy Commons

Missing Iron Problem and Type Ia Supernova Enrichment of Hot Gas in Galactic Spheroids

Shikui Tang and Q. Daniel Wang

Department of Astronomy, University of Massachusetts, Amherst, MA 01003;
tangsk@astro.umass.edu and wqd@astro.umass.edu

ABSTRACT

Type Ia supernovae (Ia SNe) provide a rich source of iron for hot gas in galactic stellar spheroids. However, the expected super-solar iron abundance of the hot gas is not observed. Instead, X-ray observations often show decreasing iron abundance toward galactic central regions, where the Ia SN enrichment is expected to be the highest. We examine the cause of this missing iron problem by studying the enrichment process and its effect on X-ray abundance measurements of the hot gas. The evolution of Ia SN iron ejecta is simulated in the context of galaxy-wide hot gas outflows, in both supersonic and subsonic cases, as may be expected for hot gas in galactic bulges or elliptical galaxies of intermediate masses. SN reverse-shock heated iron ejecta is typically found to have a very high temperature and low density, hence producing little X-ray emission. Such hot ejecta, driven by its large buoyancy, can quickly reach a substantially higher outward velocity than the ambient medium, which is dominated by mass loss from evolved stars. The ejecta is gradually and dynamically mixed with the medium at large galactic radii. The ejecta is also slowly diluted and cooled by *insitu* mass injection from evolved stars. These processes together naturally result in the observed positive gradient in the average radial iron abundance distribution of the hot gas, even if mass-weighted. This trend is in addition to the X-ray measurement bias that tends to underestimate the iron abundance for the hot gas with a temperature distribution.

1. Introduction

Soft X-ray emission of hot gas in and around galaxies depends heavily on the properties of metals (i.e., elements heavier than helium). Due to the concentrated enrichment of Type Ia supernovae (Ia SNe), the primary iron provider of the universe, hot gas in galactic stellar spheroids (galactic bulges and elliptical galaxies), in particular, is expected to have a super-solar iron abundance. Away from such a stellar spheroid, the iron-rich hot gas might be diluted by in-falling low-abundance gas. Thus a monotonically decreasing iron abundance profile as a function of galactic radius is also expected (e.g., Buote 2000a; Borgani et al. 2008) and is indeed observed on scales of the intragroup and intracluster media.

On smaller scales (within individual stellar spheroids and their immediate vicinity), however, X-ray-inferred iron abundances of the hot gas seem to be at odds with the predictions. The

abundances are typically sub-solar for low- and intermediate-mass spheroids with $\log(L_x) \lesssim 41$ to about solar for more massive ones (e.g., Humphrey & Buote 2006), substantially less than what are expected from the Ia SN enrichment. Furthermore, a number of galaxies show a significant iron abundance drop toward their central regions, where the stellar feedback should be the strongest. Examples of this abundance drop include M87 (Gastaldello & Molendi 2002), NGC 4472, NGC 5846 (Buote 2000a), and NGC 5044 (Buote et al. 2003). The inward drop of the iron abundance and its low value in general are so far not understood, which may indicate that only a small portion of metals produced by Ia SNe is observed, while the rest is either expelled or in a state that the present X-ray data are not sensitive to.

Brighenti & Mathews (2005) have explored the possibility that the iron produced by Ia SNe may have radiatively cooled and may then have avoided the detection. Based on a 1-D modeling of Ia SN remnant (SNR) evolution, they have demonstrated that the iron-rich ejecta may cool rapidly to low temperatures because of its large radiative emissivity. This scenario assumes that the cooling occurs within a critical time scale for the ejecta to be mixed microscopically with the ambient medium to an iron abundance below about 100 solar. This critical time scale is not determined, but should partly depend on the uncertain magnetic field strength and configuration, which can substantially affect the effectiveness of the iron diffusion. The mixing, of course, can also be dynamic in the violent environment of galactic stellar spheroids.

We have studied the Ia SNR evolution in a more realist setting. We have conducted 3-D hydrodynamic simulations of hot gas in a typical galactic stellar spheroid of an intermediate-mass (i.e., a galactic halo mass $M_h \sim 10^{12} M_\odot$) in a relatively isolated environment. The hot gas is expected to be in a galaxy-wide outflow, either supersonic or subsonic, depending largely on the feedback history of the galaxy (Tang et al. 2009a). Tang et al. (2009b) have presented simulations for the supersonic outflow case and have discussed several important 3-D effects: (1) SN ejecta is not well mixed with the ambient medium, and soft X-ray emission arises primarily from relatively low temperature gas shells associated with SN blastwaves; (2) The inhomogeneity in the gas temperature substantially alters the emission spectral shape, which can lead to an artificially lower iron abundance (by a factor of 2-3) in a spectral fit with a simplistic thermal plasma model; (3) The average 1-D and 3-D simulations give substantially different radial temperature profiles (e.g., the inner temperature gradient in the 3-D simulation is positive, mimicking a "cooling flow"); (4) The inhomogeneity also enhances the diffuse X-ray luminosity by a factor of a few.

In the present work, we focus on the evolution of SN ejecta and its effect on the average iron abundance measurements of the hot gas in both supersonic and subsonic outflow cases. We use the 3-D simulations to study the dilution of Ia SN iron ejecta by the stellar mass loss and the dynamic mixing with the ambient medium as well as the bulk radial outflows at abundance-dependent velocities. We demonstrate that the dropout of the iron ejecta is unlikely to be important because of the effective dynamic mixing and dilution. But the differential outflows and their gradual mixing can naturally result in an iron abundance profile qualitatively similar to what is observed. The non-uniformity of the iron abundance in the flow could also lead to an underestimate of the globally

averaged iron abundance in X-ray spectral measurements. These effects are in addition to the bias that is caused by the broad temperature distribution of the hot gas considered in Tang et al. (2009b), where only supersonic outflows are simulated and a uniform solar abundance is assumed for mock X-ray spectral analysis.

The rest of the paper is organized as follows: We first describe in § 2 our model inputs and simulation setups and then present in § 3 our new results; We give simple explanations for a few key phenomena in § 4 and summarize the work in § 5. Throughout of the paper, we adopt the solar metal abundances as listed in Anders & Grevesse (1989); in particular, our quoted iron mass abundances (i.e., the ratio of iron mass to hydrogen mass,) are relative to the solar value 2.6×10^{-3}.

2. Model Inputs and Simulation Setups

Ideally we should conduct the high-resolution 3-D simulations of the entire life of a galaxy. 3-D effects can be important in determining the early evolution of a galactic spheroid, especially in its starburst stage when the gas is in multiple phases (Tang et al. 2009b). But at present such a simulation is far too expensive to be performed with sufficient resolution to trace the detailed chemical enrichment. Thus, we have modeled the evolution of large-scale gaseous outflows in 1-D simulations to capture the global hot gas dynamics around the galaxies (Tang et al. 2009b). In the present paper, we focus on 3-D effects of the Ia SN enrichment in the globally established hot gas outflows in a region of a few kpc radius around the center of a spheroid to facilitate potential direct comparison with X-ray observations. Across this region, the dynamic time scale is short, allowing for detailed 3-D simulations. We find that the 3-D effects are important for small-scale density, temperature, and abundance structures, but have little impact on the global average dynamics of the outflows. Therefore, our approach is self-consistent.

The present investigation is based primarily on two 3-D simulations of hot gas in galaxy-wide outflows driven by Ia SNe in galactic stellar spheroids. The supersonic case corresponds to the bulk outflow that reaches a sonic point (at radius ~ 1.4 kpc), whereas the subsonic one does not. The basic setup for these two cases is the same; the model parameters are listed in Table 1. The only difference between the two is the setup of the initial conditions: the supersonic case starts

Table 1. Basic Model Parameters

Parameter	Value
Present Mass loss rate ($M_\odot$ yr^{-1})	0.075
Present energy input rate ($\mathrm{erg\,s}^{-1}$)	1.2×10^{40}
Bulge stellar mass M_* ($M_\odot$)	3×10^{10}
Bulge scale r_b (kpc)	0.7
Halo mass M_h ($M_\odot$)	10^{12}

from the 1-D solution, similar to what is presented in Tang et al. (2009b), whereas the subsonic case starts from the final output of a 1-D simulation, which includes the evolution of the circum-galactic medium in a more realistic context of galaxy evolution (Model VE; Tang et al. 2009a). By comparing results from the two cases, we intend to illustrate the dependence of the iron ejecta evolution on the global outflow speed.

Both the gas mass and the mechanical energy injections are assumed to follow the same smooth distribution as the stars, which is a Hernquist profile (Hernquist 1990) with the characteristic radius of r_b. The uncertainties in the mass and energy injection rates are a factor of ~ 2, depending on specific empirical calibrations, potential mass-loading from cool gas, etc. (e.g., David et al. 2006; Tang et al. 2009a and references therein). Our chosen energy rate is on the lower side of the uncertainty range, whereas the mass rate is on the higher side. These choices result in on average a lower gas temperature, a greater soft X-ray emissivity, and a lower iron abundance, which are more close to what are directly inferred from X-ray observations. In particular, existing studies have shown that the soft X-ray luminosities of spheroids are typically substantially higher than those predicted by the supersonic wind model, indicating that hot gas may most likely be in subsonic outflows Tang et al. (2009a,b). However, this conclusion is still very tentative; a more careful systematic analysis of existing data is required. For low- or intermediate-mass spheroids, the soft X-ray contribution from faint cataclysmic variables and coronally active binaries becomes important, which needs to be carefully subtracted. Indeed, the very faint diffuse X-ray emission from NGC 3379 after the subtraction of this contribution seems to be consistent with the superwind model (Trinchieri et al. 2008). Therefore, our simulations of both the supersonic wind and the subsonic outflow should provide a qualitative characterization of the 3-D effects on the Ia SN chemical enrichment of hot gas for both low- and intermediate-mass spheroids. The 1-D models also assume an instantaneous mixing between the ejecta and stellar mass injection and hence a uniform iron abundance of 2.7 solar. We have ignored any feedback from the supermassive black hole expected to be present at the center of a spheroid. This feedback, likely occurring in bursts with certain preferential directions (e.g., in form of jets), can occasionally result in significant disturbances in global hot gas distributions, as reflected by the asymmetric X-ray morphologies observed in some elliptical galaxies (Diehl & Statler 2008). But, averaged over the time, Ia SNe are energetically more important for a low- or intermediate-mass spheroid with $L_K \lesssim 10^{11} L_{\odot K}$ (David et al. 2006).

The simulations are performed with FLASH (Fryxell et al. 2000), an Eulerian astrophysical hydrodynamics code with the adaptive mesh refinement (AMR) capability. The 3-D simulated box, 128 kpc on a side, is centered on the spheroid and has the so-called outflow (sometimes called zero-gradient) boundary condition. As in Tang et al. (2009b), only one octant of the box is simulated at full resolution (down to about 4 pc), while the resolution is degraded by a factor of four in the rest of the grid, except for regions where SNRs seeds have just been embedded. The difference in the resolution between the regions of the same simulation allows us to check the resolution effect (e.g., on the X-ray luminosity), which appears to be rather small. In the 3-D simulations, the Ia SN injection follows the star distribution only statistically (Tang et al. 2009b). For each

"randomly" generated SN, its remnant seed is extracted from a library of 1-D simulated radial density, temperature, and velocity profiles and is scaled appropriately before being planted into the 3-D simulations (Tang & Wang 2005, 2009).

We evolve the two simulations till the averaged radial profiles of the density, pressure, and abundance have reached a statistically steady state inside the galactic radius of 10 kpc. For any quantitative analysis, we will use only the data within this radius to avoid any potential artifacts introduced by the chosen boundary condition, in the high-resolution octant, and during the final stabled period.

For the calculation of the X-ray emission and the cooling of the hot gas, we use the MEKAL plasma model (Mewe et al 1985; Liedahl et al. 1995), extracted from the XSPEC package. The cooling function of the gas is divided into the iron-free part $\Lambda_{\mathrm{noFe}}(T)$ and the pure iron rate $\Lambda_{\mathrm{Fe}}(T)$, which are shown in Fig. 1 (see also Brighenti & Mathews 2005).

3. Results

Fig. 2 shows a sample snapshot of our simulated subsonic outflow, with perspectives on the density, temperature, pressure, and iron mass fraction distributions across one plane cutting through the simulated box. The highly structured distributions of the hot gas are similar to those seen in the supersonic case (§ 1; Tang et al. 2009b), although features in the subsonic case tend to be more compact because of its higher average gas density. Time-sequenced close-ups of a region near the center of the subsonic outflow is presented in Fig. 3, demonstrating the evolution of several SNRs as well as the bulk motion. The feature labeled with "A" in the upper left panel, for example, represents the iron core of a newly embedded SNR. As indicated in subsequent panels, the iron core is gradually diluted by the local mass injection from evolved stars. In the mean time, the shapes of the core as well as the outer shell are strongly affected by the impacts of nearby SNRs (lower row). Because of both the dilution and the mixing with the surrounding medium, the iron abundance of the core is reduced to about 10 solar after about 1.5 Myr (right panel). This time scale is much too short to allow for significant cooling of the ejecta. Due to the limited spatial resolution of the simulations, the resultant iron distribution should be slightly more diffusive than the reality. But the iron mixing appears to be dominated by the random impacts or gas turbulence. In fact, we find no significant difference between the iron distributions extracted from the low and high resolution octants.

Fig. 4 shows various averaged number density, temperature, and pressure profiles extracted from the two simulations. As expected, the profiles for the subsonic outflow are much flatter than those for the supersonic ones. The difference in the density, for example, is about one order of magnitude at large radii. The profiles of the hot gas components in four iron abundance ranges show interesting differences and similarities. In general, the higher the abundance of a gas component is, the smaller the number density or the higher the temperature is. Except for the component
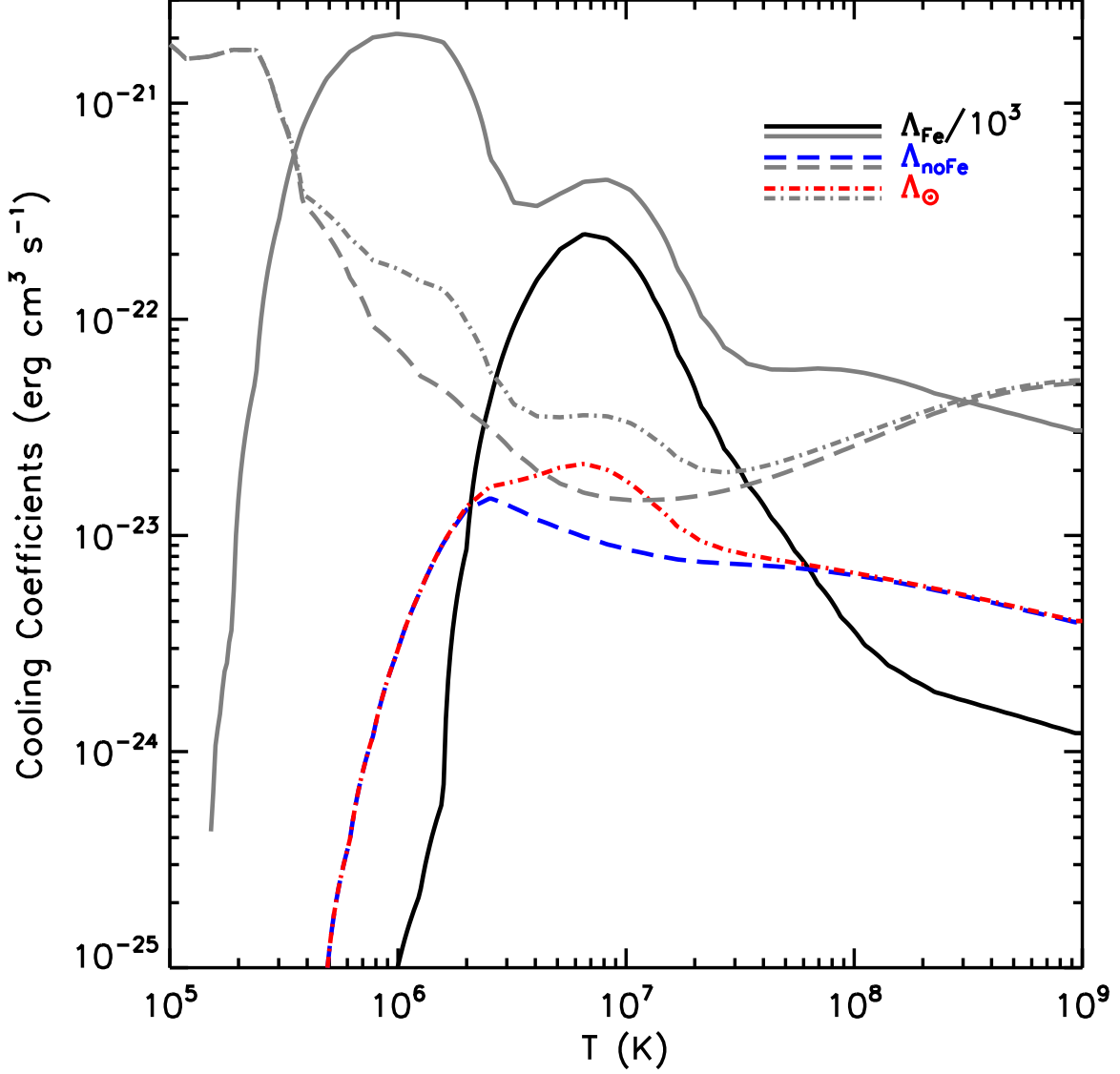
Fig. 1.— Radiative coefficients of optically-thin thermal plasma with various abundance compositions: pure iron (Λ_{Fe}, which is decreased by a factor of 10^3 for easy visualization; solid lines), solar abundance without iron (Λ_{noFe}; long-dash lines), and solar abundance ($\Lambda_\odot$; dash-dot lines). All these coefficients are constructed from XSPEC using the MEKAL model. The black and colored lines denote the coefficients in 0.3-2.0 keV band, while the corresponding gray lines are in the bolometric band. Note that $\Lambda_\odot = \Lambda_{\mathrm{noFe}} + 4.68 \times 10^{-5} \Lambda_{\mathrm{Fe}}$.
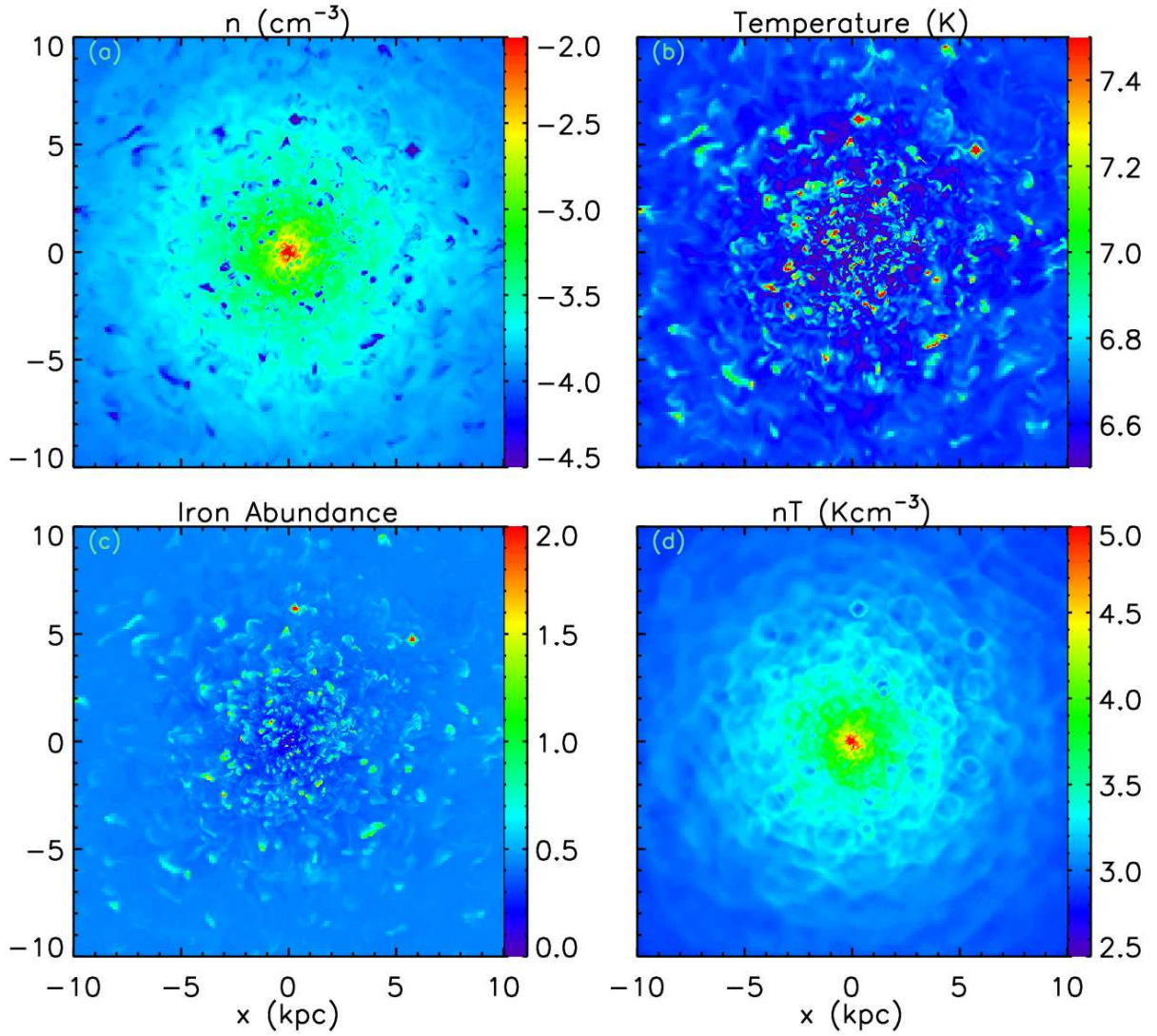
Fig. 2.— Snapshot of the 3-D simulated subsonic outflow in the z = 8 pc plane, showing the density (a), temperature (b), iron abundance (c), and pressure of the gas (d). All plots are logarithmically scaled according to the color bars. Note that the upper right quarter region in each panel denotes the data from the octant at full resolution.
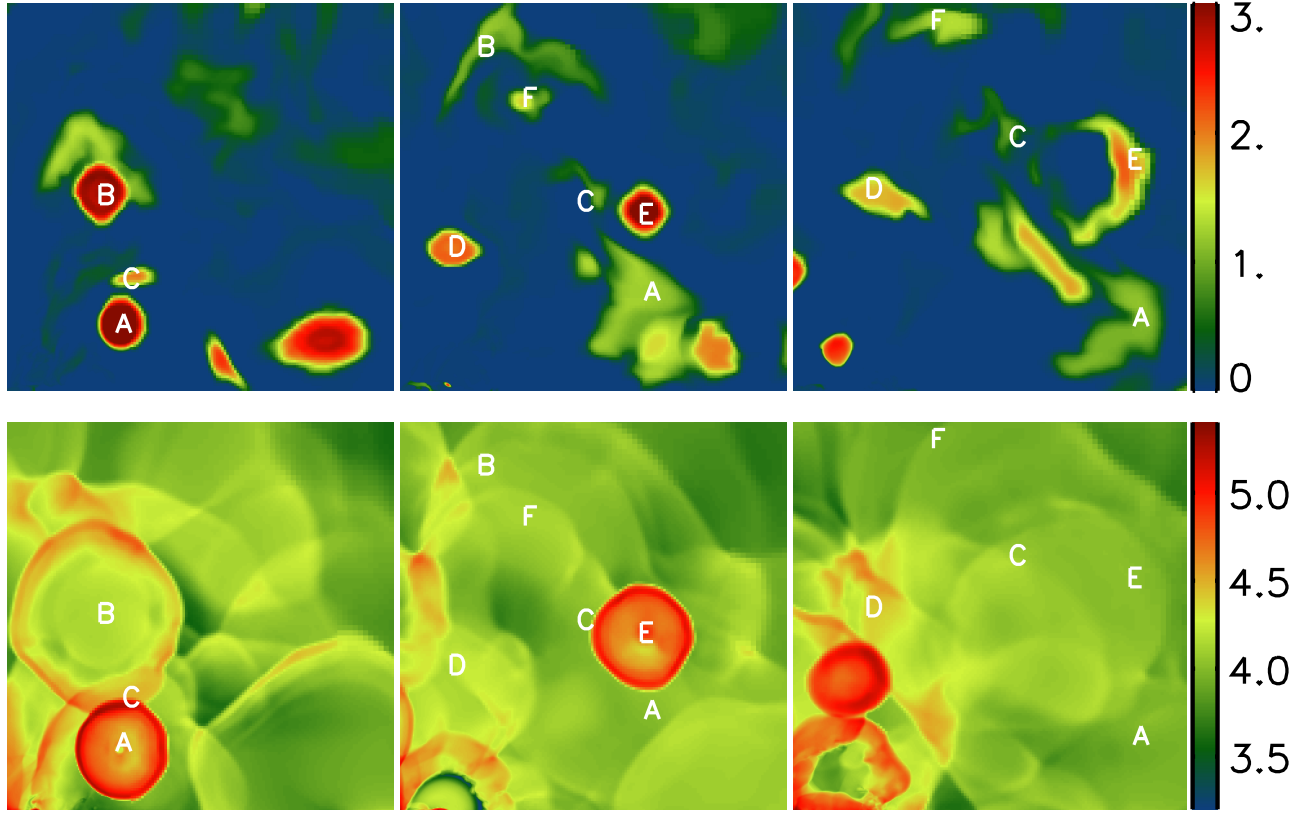
Fig. 3.— Close-ups of SNR evolution: iron abundance mostly sensitive to SN ejecta (upper row) and pressure sensitive to outer blastwave shells (lower row). The color scales are plotted logarithmically. The three panels in each row represent the same physical area of 0.6 kpc × 0.6 kpc; the low left corner of each panel is projected to the center of the model spheroid; the middle and right panels are snap-shots taken 0.86 and 1.52 Myr later after the left one. Features that orignated from the same SN ejectors are marked with the same letters in the panels. The apparent systematic motion of the features to the right and/or top of the area, as seen from the left to right panels, is due to the bulk outward flow of the hot gas. The brightest circular red disk in the lower right panel represents a remnant that is cut on a side that does not cross the SN iron ejecta and thus does not show up in the upper right panel.

with the highest abundance, the other components all have similar pressure profiles. This means that the bulk of the gas is approximately in a pressure equilibrium, although the temperature and density distributions may still be highly structured. Similar phenomena are also reported for simulations of the SN dominated interstellar medium in the Galaxy (de Avillez & Breitschwerdt 2005; Mac Low et al. 2005; Joung & Mac Low 2006) and in starburst regions (Joung et al. 2008).
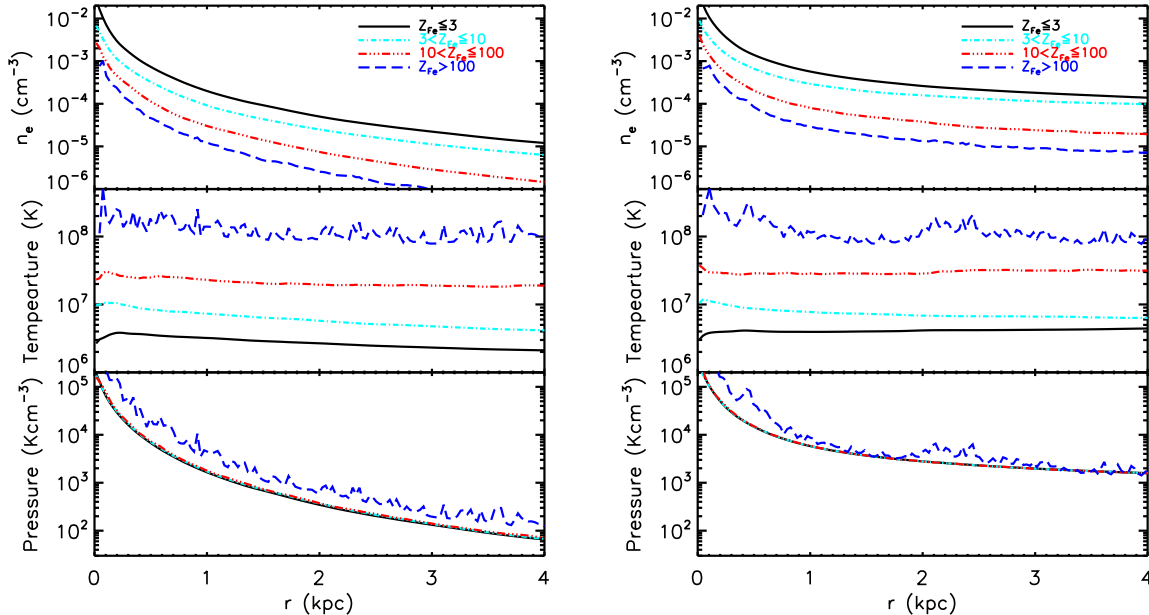

Fig. 4.— Average radial electron number density, temperature, and pressure profiles for the supersonic (left panel) and subsonic (right panel) cases. The profiles are plotted separately for the gas components with different iron abundances: $Z_{\rm Fe} \leq 3$ (solid black line), $3 < Z_{\rm Fe} \leq 10$ (dash-dot cyan line), $10 < Z_{\rm Fe} \leq 100$ (dash-three-dots red line), and $Z_{\rm Fe} > 100$ (long-dash blue line).

Fig. 5 demonstrates that gas with higher iron abundance generally has a larger net outward radial velocity. The velocity of the gas component with $Z_{\rm Fe} > 100$ fluctuates greatly, because it represents young SNRs which may or may not have been fully accelerated by the buoyancy (see § 4.2). The gas component with $10 < Z_{\rm Fe} \leq 100$, representing fully-accelerated and evolved SNRs with moderate dilution, has the largest velocity.

Fig. 6 shows the iron mass fractions of the individual gas components in the different abundance ranges. The fractions in iron-rich components decrease considerably faster with increasing radius in the subsonic case than in the supersonic one. This is because the outflow velocity is much slower in the former case, leading to more dilution and mixing of the iron ejecta before moving to large galactic radii.

Fig. 7 presents the radial profiles of the averaged iron abundance, weighted by three means.
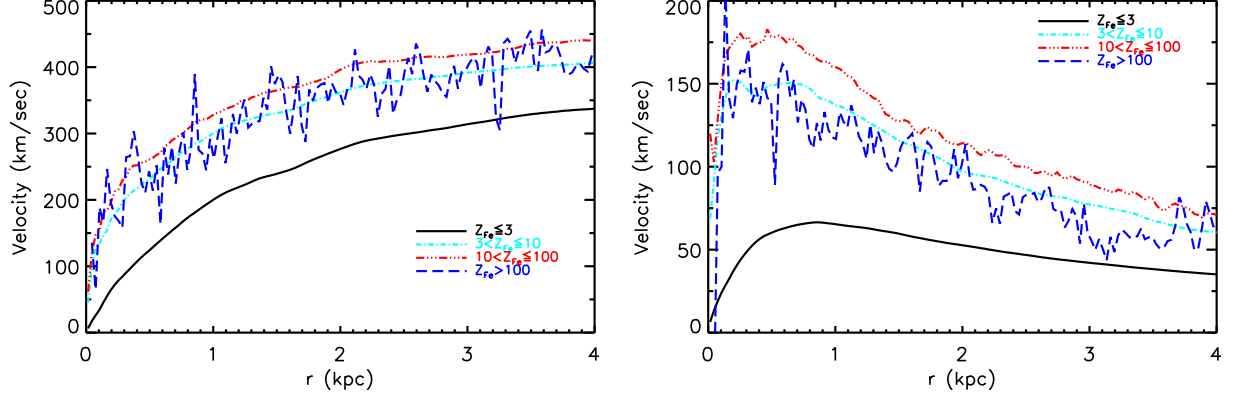
Fig. 5.— Average radial velocity profiles of the gas components with different iron abundances for the supersonic (left) and subsonic (right) cases. The line styles are the same as those in Fig. 4.
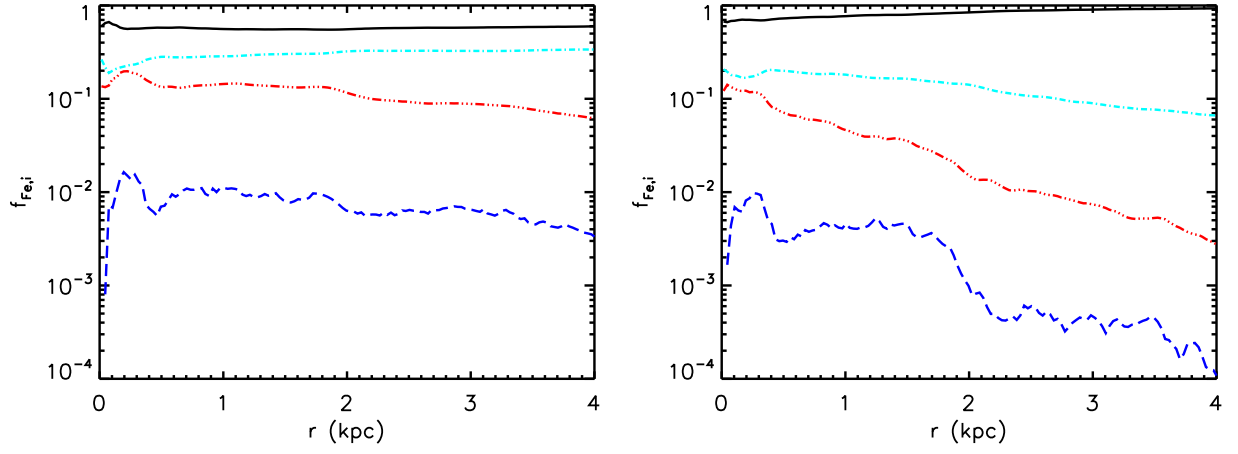

Fig. 6.— Average radial iron mass fractions of the individual gas components in the different abundance ranges for the supersonic (left) and subsonic (right) cases. The fractions are relative to the total iron mass, which includes the iron mass from stars. The line styles are the same as those in Fig. 4.

The mass-weighted iron abundance, defined as

$$< Z_{\rm Fe,mw} >= \frac{\sum_i f_i \rho_i \Delta V_i}{\sum_i \rho_i \Delta V_i} \tag{1}$$

where f_i and ρ_i is the iron mass abundance and mass density in a simulated sub-volume ΔV_i, while the sum is over an interested region (e.g., a shell). $< Z_{\rm Fe,mw} >$ is thus directly proportional to the iron mass in the region. Similarly, we can define the emission measure-weighted iron abundance as

$$< Z_{\rm Fe,emw} >= \frac{\sum_i f_i n_{e,i} n_{H,i} \Delta V_i}{\sum_i n_{e,i} n_{H,i} \Delta V_i}, \tag{2}$$

where the electron number density $n_{e,i}$ is related to the hydrogen number density $n_{H,i}$ (hence ρ_i) and the $Z_{Fe,i}$ in the same way as described by Brighenti & Mathews (2005). $< Z_{\rm Fe,emw} >$ probably represents the simplest way to estimate the equivalent abundance that can be compared with an actual measurement based on X-ray emission. An alternative model proxy to the X-ray emission-inferred value is the emission-weighted iron abundance,

$$< Z_{\rm Fe,ew} >= \frac{\sum_i f_i n_{e,i} (n_{H,i} \Lambda_{\rm noFe} + n_{\rm Fe} \Lambda_{\rm Fe}) \Delta V_i}{\sum_i n_{e,i} (n_{H,i} \Lambda_{\rm noFe} + n_{\rm Fe} \Lambda_{\rm Fe}) \Delta V_i}. \tag{3}$$

In our simulations, the $<Z_{\rm Fe,ew}>$ might be overestimated at large radii because SN iron cores are not adequately resolved (i.e., the spatial resolution in regions of $r > 5\,{\rm kpc}$ is reduced by a factor of four), which numerically mixes the iron ejecta over a larger volume and effectively results in a higher n_e (hence stronger emission). Fig. 7 shows that the radial trends of these differently weighted iron abundances are qualitatively the same: a positive gradient with a minimum value at the center! The lower limit of the abundance is solar, assumed for the stellar mass loss.

4.   Discussion

Here we attempt to give a physical account of several key phenomena observed in the simulations presented above.

4.1.   Thermal Evolution of Ia SN Iron Ejecta

We find no evidence for significant cooling of the hot gas, especially the iron ejecta, in our simulated region. To have a better understanding of this issue, it is instructive to first consider a simple 1-D simulation of a typical SNR in a hot gas environment, as in Brighenti & Mathews (2005), but in the context of an intermediate-mass spheroid considered here (Tang & Wang 2005). As mentioned in § 2, the 1-D simulated SNR is also used to generate the seeds for the 3-D simulations. Fig. 8 demonstrates the simulated SNR evolution in a uniform ambient medium of temperature $T_0 = 10^7\,{\rm K}$ and electron density $n_e = 0.01\ {\rm cm}^{-3}$, appropriate for a region near the center of the
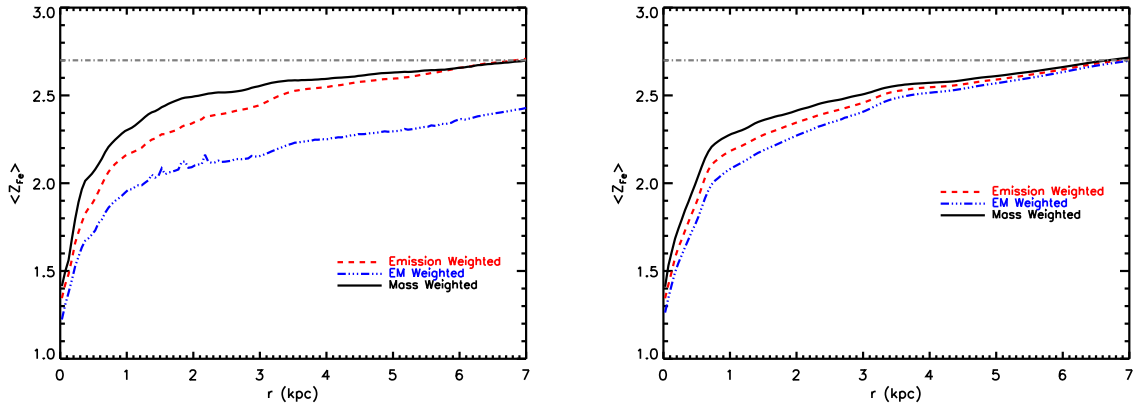
Fig. 7.— Average radial iron abundance profiles for the supersonic (left panel) and subsonic (right panel) cases. The profiles weighted by mass, emission, and emission measure are plotted separately as labeled. The horizontal dash-dot gray line denotes the expected abundance if iron ejecta is uniformly mixed with stellar mass loss materials.

spheroid. The core that encloses $0.7\,M_\odot$ reaches a size of $15\,\mathrm{pc}$ at the age of 10^4 years and increases only slightly after that. This is also roughly the time scale for the ejecta to be fully thermalized by the converging reverse shock. Then the core turns into a tenuous hot bubble, with a very low density and high temperature. Outside the iron core is an envelope of the rest of the SN ejecta (assumed to be $0.7\mathrm{M_\odot}$). The swept-up material can also be heated to more than $10^8\,\mathrm{K}$ only initially by the strong forward blastwave; the averaged temperature of the swept-up material is considerably lower because of the quick weakening of the expanding blastwave and the adiabatic cooling of the SNR. The radiative cooling time scale (Fig. 9) for such an SNR is much too long to be important, compared to the outflow time of the hot gas from a spheroid ($\lesssim 10^7$ yrs). In particular, the X-ray emission from the ejecta is largely undetectable.

We now consider additional processes that an SNR should experience in a spheroid. One is the dilution due to mass injection from evolved stars (or evaporation of cloud-lets). As the dilution takes place, n_e increases while $\Lambda_{\mathrm{Fe}}(T)$ drops. The net result is that the cooling rate peaks when the iron abundance drops to ~ 100 solar (Brighenti & Mathews 2005). Further dilution tends to decrease the cooling rate. Take the above 1-D SNR as an example. It takes about $2.7\,\mathrm{Myr}$ for the SNR core to accumulate an additional $5.4\ M_\odot$, which dilutes the ejecta to an iron abundance of 100 solar, the value to avoid rapid radiative cooling (Brighenti & Mathews 2005). In comparison, the time for the SNR to flow this radius to $2\,\mathrm{kpc}$ is about $5\,\mathrm{Myr}$. Thus the dilution is important, although the core should still have a high iron abundance when being transported out of the spheroid. Another process is the mixing of the iron ejecta with the ambient medium. The density of bulk of the SNR interior is always smaller than the surrounding medium, as demonstrated in the 1-D modeling, and is likely subjected to the Rayleigh-Taylor instability (e.g., Sedov 1959; Wang & Chevalier 2001).
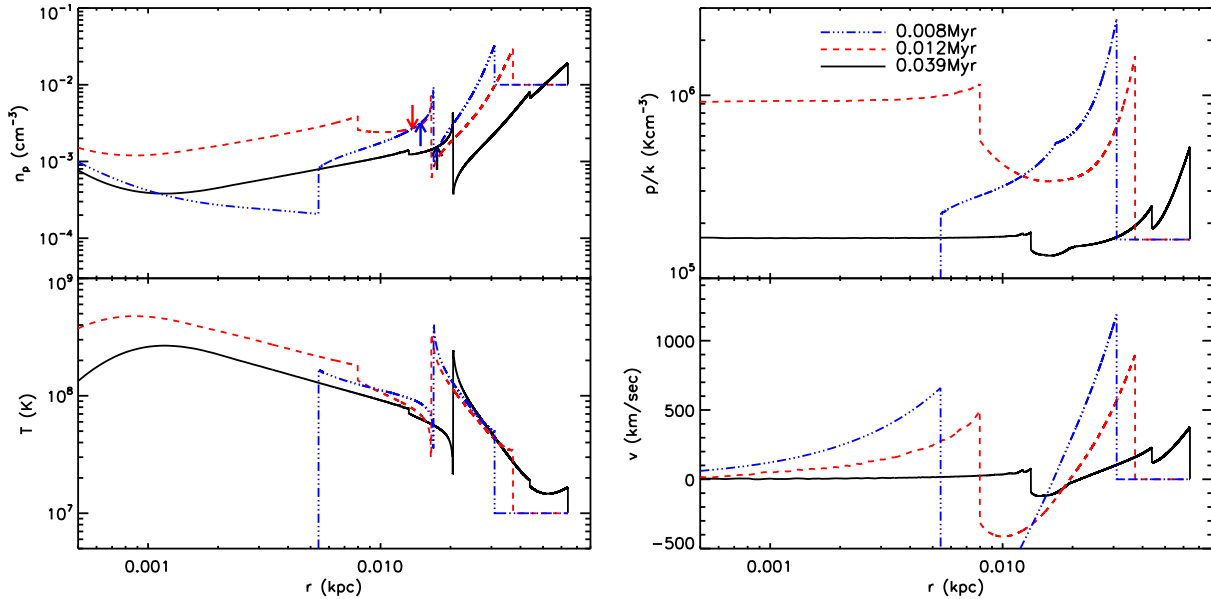
Fig. 8.— Sample density, temperature, pressure, and velocity profiles of an SNR at three different ages: 8×10^3 yr (dash-three-dots blue line), 1.2×10^4 yr (dash red line), 3.9×10^4 yr (solid black line). The arrows in the density panel denote the outer radii of the iron ejecta.

The passage of blastwaves produced by nearby SNe also tends to accelerate the mixing process, especially in the inner spheroid region where the stellar density is very high. Our Euler-based hydrodynamical simulations account for this cooling rate effect as well as the dilution and mixing processes.

We conclude that the radiative cooling of the iron ejecta is unlikely to be important in the type of spheroids we have considered. But we cannot rule out the possibility that Ia SN ejecta may cool and drop off from hot gas in a more quiescent environment. In a giant elliptical galaxy considered by Brighenti & Mathews (2005), hot gas density can be rather high, substantially increasing the cooling, and the bulk motion may not be significant. Unfortunately, a 3-D simulation of the hot gas in such an environment is still very difficult to conduct, because of both the large dynamic range over a big volume and the difficulty to handle the boundary condition.

4.2. Buoyancy-Driven Dynamics of the Ejecta

One of our findings is that the differential radial outflows play an important role in determining the iron abundance profile of the hot gas. The relatively large outflow speed of the iron-rich gas is apparently caused by the presence of the buoyancy force. A reverse-shock heated SN ejecta bubble, with a density that is one to two orders of magnitude less than that of the ambient medium, is
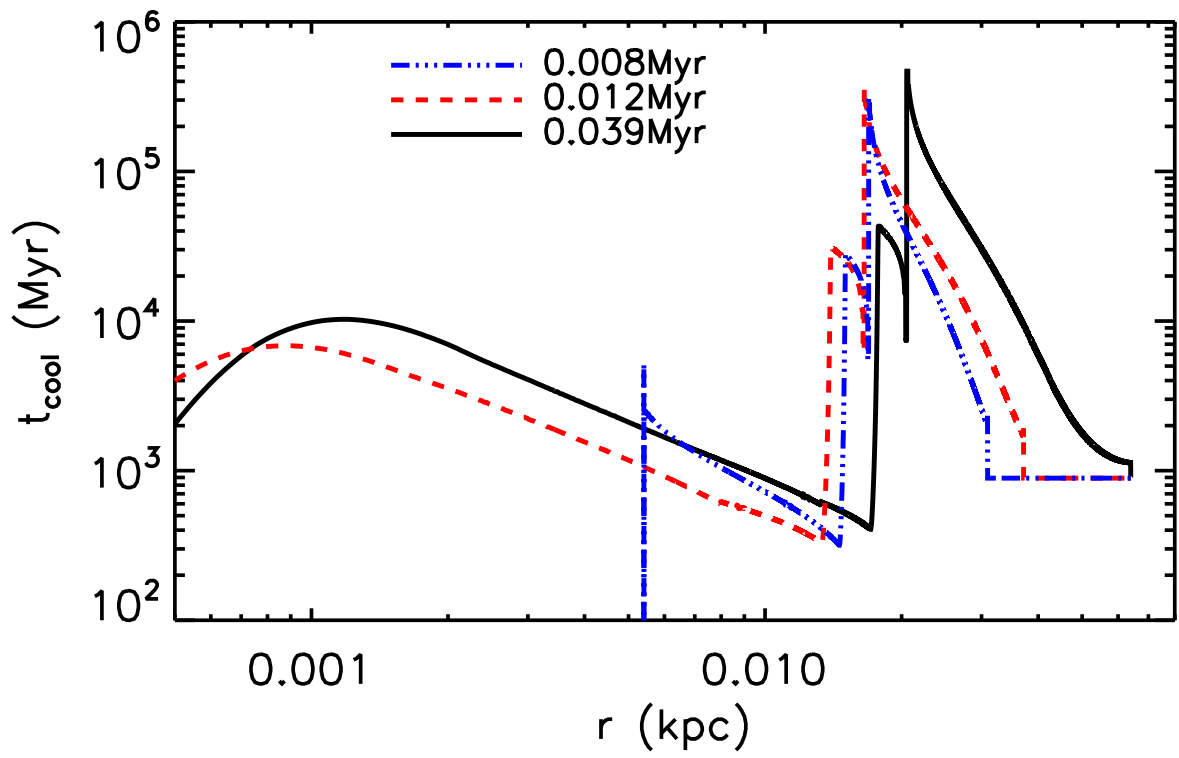
Fig. 9.— The cooling time scale as a function of radius, calculated with the profiles given in Fig. 8.

subject to a buoyancy-driven acceleration as

$$\mathbf{a}_{\mathrm{buoy}} = -\mathbf{g}\left(\frac{\bar{\rho}_{\mathrm{amb}}}{\bar{\rho}_{\mathrm{hb}}} - 1\right), \tag{4}$$

where $\mathbf{g}$ is the gravitational acceleration while $\bar{\rho}_{\mathrm{hb}}$ and $\bar{\rho}_{\mathrm{amb}}$ are the average densities of the bubble and its ambient medium. For our adopted model spheroid, $g \simeq 90\,\mathrm{km\,s^{-1}\,Myr^{-1}}$ at $0.5\,\mathrm{kpc}$, for example, and is larger near the galactic center. Assuming a typical $\bar{\rho}_{\mathrm{amb}}/\bar{\rho}_{\mathrm{hb}} \approx 10$, the hot bubble can be accelerated over a period of $0.2\,\mathrm{Myr}$ to about 150 km s^{-1}, a typical velocity difference between the iron-rich gas and the bulk of the outflow. This velocity is also about the equilibrium value that can be reached when the buoyancy force is balanced by a drag:

$$\mathbf{a}_{\mathrm{drag}} = -\hat{\mathbf{v}}_{\mathrm{hb}} \cdot \frac{1}{2}CA_{\mathrm{hb}}v_{\mathrm{hb}}^2\rho_{\mathrm{amb}}/m_{\mathrm{hb}}, \tag{5}$$

where A_{hb}, m_{hb}, and $\hat{\mathbf{v}}_{\mathrm{hb}}$ are the maximum cross-section area, mass, and velocity of the hot bubble, respectively. The coefficient C is suggested to be ~ 1 (e.g., Jones et al. 1996). The above crude estimates are consistent with the results from our detailed examination of individual hot bubbles in the simulations, which naturally account for such complications as the changing sizes and shapes as well as the decreasing density contrasts relative to the ambient medium.

4.3. Nature of the Iron Abundance Gradient

We find that the positive radial gradient of the iron abundance shown in Fig. 7 is due largely to the differential outward velocities of the gas (Fig. 5). The relative fast outward motion of the iron-rich gas naturally leads to a reduced iron mass fraction in the bulk outflow. For an illustration, suppose that a model hot gas contains only two components: the first one (sub-scripted with 1 hereafter) is iron-free, whereas the second one (sub-scripted with 2) is pure iron. These two components have outward mass fluxes at radius r:

$$F_1 = 4\pi r^2 \rho f_1 v_1, \tag{6}$$
$$F_2 = 4\pi r^2 \rho f_2 v_2, \tag{7}$$

where f and v represent the average mass fraction and outward velocity of each component, while ρ is the total mass density of the gas. The iron abundance is then

$$Z_{\mathrm{Fe}} \equiv \frac{f_2}{f_1 + f_2} \tag{8}$$
$$\simeq \frac{F_2}{F_1}\frac{v_1}{v_2}, \tag{9}$$

where $f_2 << f_1$ is adopted because the total iron mass is no more than a few percent of the total gas mass. The ratio F_2/F_1 is the same as the iron mass fraction of the injection from the stellar mass loss, independent of the spatial lumpiness in the iron distribution. Eq. 9 thus illustrates that the faster the iron-rich gas component moves relative to the rest of the outflow, the lower its mean iron abundance should be.

5. Summary and Conclusions

We have examined the evolution of Ia SN iron ejecta in the hot gas undergoing outflows from a typical intermediate-mass galactic stellar spheroid. 3-D hydrodynamic simulations of this hot gas are conducted for both supersonic and subsonic cases. These simulations show no evidence for the iron ejecta to significantly cool and drop out of the hot gas. The largely inhomogeneous enrichment and heating, inherited from sporadic Ia SNe, can significantly affect the X-ray measurement of the mean iron abundance of the hot gas in two ways:

1. Hot and low-density iron bubbles, generated by Ia SNe, tend to move outward substantially faster than the ambient medium. This differential motion, produced mainly in the inner galactic region under the strong buoyancy force, effectively reduces the mean iron abundance of the hot gas. The reduction decreases with the increasing galactic radius as the iron bubbles are gradually mixed with the ambient medium and are diluted by fresh mass injection from evolved stars.

2. Because of their high temperature and low density, the iron-rich bubbles hardly radiate, contributing little to the X-ray emission of the hot gas (Tang et al. 2009a). The bulk of the emission arises from the ambient medium swept up by SNR forward blastwaves, which has higher densities and lower temperatures. This iron segregation as well as the density and temperature distributions, most apparent again in the inner galactic region, can lead to a significant underestimate of the actual mean iron abundance of the hot gas, when characterized with a simplistic plasma model (e.g., with one- or two-temperature components).

These two effects together provide a natural explanation for the low iron abundance and its positive radial gradient, as inferred from existing X-ray measurements of hot gas in various galactic stellar spheroids. Unfortunately, a direct comparison with existing observations is still difficult. The inward drop of the iron abundance is usually observed in massive spheroids. However, this is most likely an observational bias. We are not aware of a reliable measurement of the abundance profile for low- and intermediate-mass spheroids. Not only the counting statistics is typically insufficient, but the contribution from faint cataclysmic variables and coronally active binaries becomes important as well. This contribution, in particular, is typically not subtracted in existing studies. A more careful data analysis is needed for such spheroids. The observational measurements for massive objects are easier to make and more reliable. The measurement by Buote et al. (2003), for example, shows that the iron abundance within the central ~ 4 kpc radius of NGC 5044 is on average only $\sim 2/3$ of that in the 4-12 kpc surrounding region, which is consistent with the prediction from our simulation of the subsonic outflow. However, NGC 5044 is a massive galaxy in a group, while the simulation is suited for an intermediate-mass one. Thus, a quantitative comparison would be problematic, although the 3-D effect of the buoyancy on the abundance distribution should remain the same qualitatively.

This work together with those presented in Tang et al. (2009a,b) demonstrates that X-ray observations of hot gas in and around spheroids can potentially be used as a unique tool to probe the dynamics of the feedback from evolved stars as well as SMBHs, which represents a very poorly understood part of galaxy formation and evolution theories. To reach this goal, more work is clearly needed to understand the hot gas, both theoretically and observationally. Particularly useful will be spatially-resolved high-resolution spectroscopy of the hot gas, as could be provided by the future International X-ray Observatory, as well as careful analysis of existing high-quality X-ray imaging data. But a large parameter space of the modeling also needs to be explored to facilitate quantitative comparisons with the existing and future observations.

REFERENCES

Anders E., & Grevesse N., 1989, Geochimica et Cosmochimica Acta, 53, 197

Borgani S., Fabian D., Tornatore L., Schindler S., Dolag K., Diaferio A., 2008, Space Sci. Review, 134, 379

Brighenti Fabrizio, & Mathews William G., 2005, ApJ, 630, 864

Buote D. A., 2000a, ApJ, 539, 172

Buote D. A., 2000b, MNRAS, 311, 176

Buote D. A., Lewis A. D., Brighenti F., & Mathews W. G. 2003, ApJ, 595, 151

Cioffi, D. F., Mckee, C. F., & Bertschinger, E. 1988, ApJ, 334, 252

David L. P., Jones C., Forman W., Vargas I. M., Nulsen P., 2006, ApJ, 653, 207

de Avillez M. A., & Breitschwerdt D., 2005, A&A, 436, 585

Diehl, S, & Statler, T. S. 2008, ApJ, 680, 897

Fabian D., Tornatore L., Borgani S., Saro A., Dolag K., 2008, MNRAS, 386, 1265

Fryxell B., et al., 2000, APJS, 131, 273

Gastaldello F., & Molendi S. 2002, ApJ, 572, 160

Hernquist L., 1990, ApJ, 356, 359

Humphrey P. J., & Buote D. A., 2006, ApJ, 639, 136

Ji J., Irwin J. A., Athey A., Bregman J. N., & Lloyd-Davies E. J. 2009, ApJ, 696, 2252

Jones T. W., Ryu D., & Tregillis I. L., 1996, ApJ, 473, 365

Joung M. K., Mac Low M.-M., Bryan G. L., 2008, ApJ, 704, 137

Joung M. K., & Mac Low M.-M., 2006, ApJ, 653, 1266

Liedahl D. A., Osterheld A. L., & Goldstein W. H., 1995, ApJ, 438, L115

Loewenstein M., Mathews W. G., 1987, ApJ, 319, 614

Mac Low M.-M., Balsara D. S., Kim J., de Avillez M. A., 2005, ApJ, 626, 864

Mathews, W. G., & Brighenti, F. 2003, ARA&A, 41, 191

Mewe R., Gronenschild E. H. B. M., & van den Oord G. H. J. 1985, A&AS, 62, 197

Raley E. A., Shelton R. L., Plewa T., 2007, ApJ, 661, 222

Sedov L. I 1959, Similarity and Dimensional Methods in Mechanics, translation from 4th Russian edition, Academic press New York and London

Strickland D. K., & Stevens I. R., 1998, MNRAS, 297, 747

Sutherland R. S., Dopita M. A., 1993, ApJS, 88, 253

Tang S., & Wang Q. D. 2005, ApJ, 628, 205

Tang, S, & Wang, Q. D. 2009, MNRAS, 397, 2106

Tang S., Wang Q. D., Lu Y., Mo H. J., 2009a, MNRAS, 392, 77

Tang S., Wang Q. D., Mac Low M.-M., Joung M. R. 2009b, MNRAS, 398, 1468

Trinchieri, G., et al. 2008, ApJ, 688, 1000

Wang C., & Chevalier R. A., 2001, ApJ, 549, 1119